Research Article

Jialu Wang*, Rongfei Yu, Zhenying Li, Fen Yang, Linmin Luo, Dandan Wang, Huan Cheng, Yutao Zhang*, and Qiuyun Zhang*

Heteropolyacid-loaded MOF-derived mesoporous zirconia catalyst for chemical degradation of rhodamine B

https://doi.org/10.1515/gps-2023-0005
received January 13, 2023; accepted March 28, 2023

Abstract: In this article, silicotungstic acid (STA)-loaded metal–organic framework (MOF)-derived composites (C-STA@ZrO_2) were successfully synthesized by simple strategies. X-ray diffraction, Fourier transform infrared, scanning electron microscopy, energy-dispersive X-ray, N_2 physisorption, UV-vis diffuse reflection spectroscopy, and X-ray photoelectron spectroscopy techniques were used to characterize the as-obtained composites. Intriguingly, C-STA@ZrO_2 exhibits excellent photocatalytic performance, and rhodamine B (RhB) (40 mg·L^{-1}) in water can be degraded to 93.9% after 120 min of irradiation. Moreover, various catalysts, catalyst dosage, and dye concentrations on RhB degradation were evaluated. Besides, the reusability of C-STA@ZrO_2 was also investigated. This work may provide a new and significant guideline for exploring excellent performance of MOF-derived hybrid material for wastewater purification.

Keywords: metal–organic framework, silicotungstic acid, photocatalysis, rhodamine B, photodegradation

*** Corresponding author: Jialu Wang,** College Rural Revitalization Research Center of Guizhou, School of Resource and Environmental Engineering, Engineering Technology Center of Control and Remediation of Soil Contamination of Guizhou Science and Technology Department, Anshun University, 561000, Guizhou, China, e-mail: lu226@163.com
*** Corresponding author: Yutao Zhang,** College Rural Revitalization Research Center of Guizhou, School of Chemistry and Chemical Engineering, Engineering Technology Center of Control and Remediation of Soil Contamination of Guizhou Science and Technology Department, Anshun University, 561000, Guizhou, China, e-mail: zyt0516@126.com
*** Corresponding author: Qiuyun Zhang,** College Rural Revitalization Research Center of Guizhou, School of Chemistry and Chemical Engineering, Engineering Technology Center of Control and Remediation of Soil Contamination of Guizhou Science and Technology Department, Anshun University, 561000, Guizhou, China, e-mail: sci_qyzhang@126.com
Rongfei Yu, Zhenying Li, Fen Yang, Linmin Luo, Dandan Wang, Huan Cheng: College Rural Revitalization Research Center of Guizhou, School of Chemistry and Chemical Engineering, Engineering Technology Center of Control and Remediation of Soil Contamination of Guizhou Science and Technology Department, Anshun University, 561000, Guizhou, China

1 Introduction

With the rapid development of the printing and dyeing industries, the demand for organic dyes is growing rapidly [1]. However, these organic dyes are inevitably discharged into water, which can increase the extent of environmental pollution and disturb ecosystems because of their non-biodegradability and high toxicity [2,3]. To solve these problems, various methods (e.g., physical adsorption, chemical oxidation, and biological treatment) have been studied to remove the dye-contaminated water [4–9]. Among these techniques, the photocatalysis technique has been highlighted as one of the most promising methods for wastewater remediation [10]. During the photocatalytic reaction, many photocatalysts (e.g., metal oxides, graphitic carbon nitride, and zeolites) have been widely studied [11].

Recently, heteropolyacids are receiving considerable attention in the photocatalysis field, such as silicotungstic acid (STA), phosphomolybdic acid, and tungstophosphoric acid, because of their high catalytic, unique redox properties, and electron trapping capacity; especially, the unoccupied W 5d states of the Keggin STA unit can be used as an electron trap [12,13]. Unfortunately, the practical engineering application of heteropolyacids is limited due to their high solubility in polar solvents and low surface area [14]. Therefore, several modification techniques (e.g., supporting and doping) have been investigated, aiming to solve this problem [15]. Among them, loading heteropolyacids into porous substances with high surface area is one of the most promising strategies.

Metal–organic framework (MOF), constructed from metal ions/clusters and organic linkers, has been widely

used in various fields owing to its clear porosity, large specific surface areas, and tailorability [16–19]. In particular, Zr-base MOF (e.g., UiO-66) has demonstrated excellent performance in a variety of photocatalysis reactions, due to various features, such as high defect tolerance and high hydrothermal stability [20,21]. More recently, through a simple heat treatment process, MOF can be transformed into hierarchically porous metal oxides, which is beneficial to enhance interaction between metal oxides and active components [22–24]. Thus, MOF-derived metal oxide skeletons are an ideal candidate for loading heteropolyacids. In this study, UiO-66-derived zirconia (ZrO_2) skeletons as support-loaded STA hybrids (C-STA@ZrO_2) were synthesized via a one-pot hydrothermal process followed by heat treatment strategy for visible light degradation of rhodamine B (RhB) dye. The hybrids were characterized by X-ray diffraction (XRD), Fourier transform infrared (FTIR), scanning electron microscopy (SEM), energy-dispersive X-ray (EDX), N_2 physisorption, UV-vis diffuse reflection spectroscopy (DRS), X-ray photoelectron spectroscopy (XPS), etc. Furthermore, the stability of C-STA@ZrO_2 and the possible degradation mechanism were also explored.

2 Materials and methods

2.1 Reagents

Zirconium(IV) chloride ($ZrCl_4$), terephthalic acid (H_2BDC), silicotungstic acid (STA, $H_4SiW_{12}O_{40}{\cdot}nH_2O$), *N*,*N*-dimethylformamide (DMF), absolute ethanol, RhB, congo red (CR), acridine orange (AO), and methylene blue (MB) were obtained from Sigma-Aldrich. All reagents were of analytical grade and were used directly without any further purification.

2.2 Synthesis

STA-loaded MOF-derived ZrO_2 was prepared through a sample way. Briefly, H_2BDC (2 mmol, 0.3323 g), $ZrCl_4$ (1 mmol, 0.233 g), and STA (0.3 g) were dissolved in 18 mL ethanol and kept for 10 min under ultrasound conditions and subsequently stirred for 60 min at ambient temperature. Then, the aforementioned mixture was transferred into an autoclave and heated at 150°C for 6 h. After the autoclave was cooled, the resulting precipitate was centrifuged and washed with DMF and deionized water three times. Finally, the obtained samples were dried and annealed at 350°C for 2 h with the heating rate of 5°C·min^{-1}, and the hybrid material was marked as C-STA@ZrO_2. Besides, the synthesis route of C-STA@ZrO_2 composite is presented in Scheme 1. In addition, C-ZrO_2 without adding STA was fabricated using a similar process.

2.3 Characterization techniques

The XRD patterns were identified by D8 ADVANCE (Germany) using CuKα (1.5406 Å) radiation in the 2θ range of 5–65°. FTIR spectra were measured to determine the chemical features of the samples on a PerkinElmer spectrum 100 using KBr pellet technology (4,000–400 cm^{-1}). The particle sizes and morphologies of the catalysts were observed using SEM (Hitachi S-4800, Japan), and element distribution was obtained on EDX. The surface area and particle sizes of the as-obtained samples were measured by N_2 adsorption and desorption isotherms using a Quantachrome Quadrasorb EVO apparatus (Quantachrome Instruments, Boynton Beach, USA). UV-vis diffuse reflectance spectroscopy of the as-obtained samples was recorded through UV-vis spectrophotometer (Shimadzu, UV-3600 PLUS, Japan).

2.4 Photochemical reactions

The photocatalytic performance of the as-obtained catalysts toward organic pollutant degradation was evaluated under visible light irradiation at room temperature. Typically, 0.05 g catalyst was mixed with 50 mL of 40 mg·L^{-1} RhB aqueous solution. Before photodegradation, the solution was stirred in the dark for 30 min to ensure the adsorption equilibrium. Then, the resulting solution was irradiated

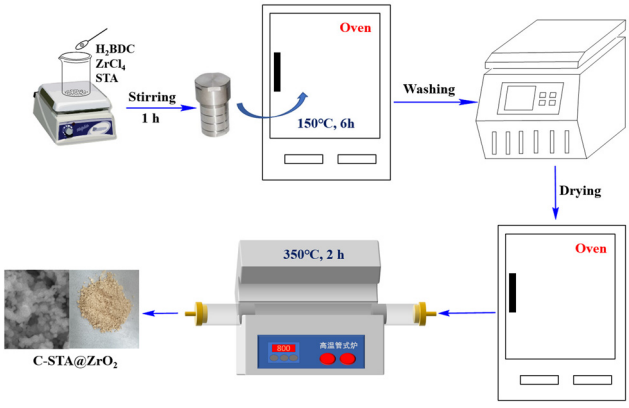

Scheme 1: Synthesis route of C-STA@ZrO_2 composite.

with a 300 W xenon arc lamp for 2 h. At specific time intervals, a sample of 3–4 mL was taken out, centrifuged, and analyzed by a UV-5200 PC spectrophotometer at the characteristic wavelength. To evaluate the reusability, the catalyst was separated by centrifugation after each use, washed with DMF, and vacuum-dried overnight for the next photodegradation. Moreover, the photodegradation rate of RhB could be calculated by the following equation:

$$R(\%) = (1 - C/C_0) \times 100\%, \quad (1)$$

where C_0 is the initial concentration of RhB and C is the concentration of RhB after "t" minutes illumination, respectively.

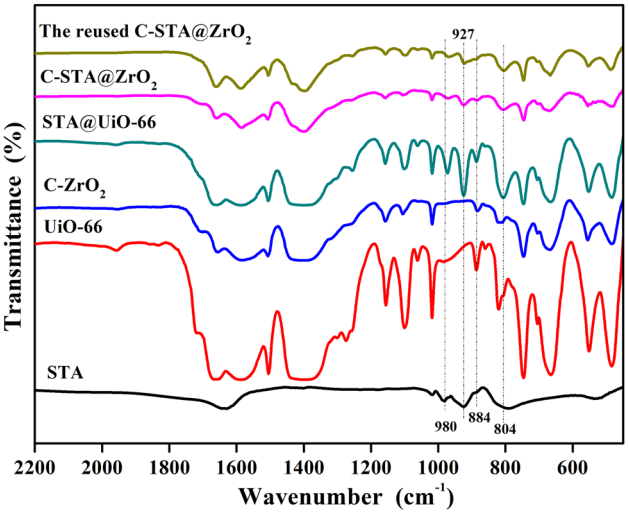

Figure 1: FTIR spectra of obtained photocatalysts.

3 Results and discussion

3.1 Characterization

The XRD diffractograms of STA, UiO-66C-ZrO_2, STA@UiO-66, and C-STA@ZrO_2 catalysts are shown in Figures A1 and A2 (in Appendix). According to Figure A2, UiO-66 has two distinct characteristic peaks at 7.3° and 8.5° corresponding to crystal planes (111) and (200), indicating that UiO-66 is successfully synthesized [25]. As shown in Figure A1, it is worth noting that the XRD diffraction peaks of C-ZrO_2 and STA@UiO-66 catalysts are similar to that of UiO-66, which is attributed to the similar structural features. It also indicates that the crystal structure of UiO-66 is well maintained during the pyrolysis process and the introduction of STA. As STA@UiO-66 is calcined at 350°C, C-STA@ZrO_2 shows the diffraction peak position similar to the C-ZrO_2 catalyst, indicating that the C-ZrO_2 and C-STA@ZrO_2 have the same structure. However, compared to C-ZrO_2, the peak intensities were slightly weaker for the C-STA@ZrO_2 sample, which may be due to the interaction between the generation of zirconia (ZrO_2) and STA [26]. In addition, no evident STA peaks were observed in the STA@UiO-66 and C-STA@ZrO_2 hybrids; it was possible due to the STA being well dispersed on the framework structure [27]. According to the XRD analysis results, the successful synthesis of STA-loaded MOF-derived ZrO_2 catalyst was performed.

The FTIR spectra patterns of the STA, UiO-66, C-ZrO_2, STA@UiO-66, and C-STA@ZrO_2 catalysts are presented in Figure 1. The FTIR spectra of STA have four distinct absorption peaks at 804, 884, 927, and 980 cm^{-1}, corresponding to the Keggin structure of STA. Notably, all peaks of UiO-66 that appeared in the FTIR spectra are well agreed with those previously reported [28], which confirmed that UiO-66 had been successfully synthesized. Compared to UiO-66, the FTIR spectra of C-ZrO_2 and C-STA@ZrO_2 are similar to that of UiO-66, but the intensity of all bands decreases greatly after the pyrolysis, which may be due to the partial decomposition of the organic ligand and the generation of ZrO_2. Moreover, the characteristic absorption peaks of STA are found in the STA@UiO-66 and C-STA@ZrO_2 hybrids, which is evident that the STA groups were attached to UiO-66 and the skeleton structure of STA was not decomposed during pyrolysis process, and this is consistent with XRD results.

SEM analysis in Figure 2 showed the morphological features of the synthesized UiO-66, C-ZrO_2, and C-STA@ZrO_2 catalysts. As shown in Figure 2a, UiO-66 exhibits spherical particles with aggregation nature. Compared to morphology of UiO-66 before and after calcination, sintering and the shrinkage of particles occurred, resulting in the formation of sphere-shaped particles with a size of about 200 nm for C-ZrO_2 (Figure 2b). When the STA is introduced, it can be seen from Figure 2c and d that C-STA@ZrO_2 catalyst was messy and rough with an irregular dimensional nearly sphere-like shaped particles, and the obvious pore structure and aggregation could be observed. This phenomenon may be explained by the presence of strong interaction between STA and ZrO_2 after thermal transition process, which may cause an important effect on the surface morphology. Simultaneously, it is also noted that the presence of pore structure can decrease the recombination rate of electron–hole pairs and is further beneficial for photocatalysis applications [29]. Besides, the elements of the prepared C-STA@ZrO_2 catalyst were verified by EDS, and it can be seen from Figure 2e that Zr and W elements existed

in the sample, suggesting the successful preparation of the C-STA@ZrO_2 composite.

The optical properties of the synthesized C-ZrO_2 and C-STA@ZrO_2 catalysts were assessed by UV-vis DRS analysis. As shown in Figure 3a, C-ZrO_2 and C-STA@ZrO_2 exhibited strong absorption responses in the visible light region (200–800 nm). The maximum absorption band edges of C-ZrO_2 and C-STA@ZrO_2 are about 338 and 440 nm, respectively, illustrating that the impregnation of STA could effectively improve the optical response range of C-ZrO_2. In addition, the optical bandgap of catalyst can be estimated from the Tauc plot method [30]. As illustrated in Figure 3b, the bandgap values (E_g) of the materials were calculated to be 3.93 and 3.11 eV for C-ZrO_2 and C-STA@ZrO_2, respectively. It could be distinctly observed that the C-STA@ZrO_2 displayed an obvious red shift compared with C-ZrO_2, revealing the interaction between STA and ZrO_2 in the C-STA@ZrO_2 heterostructure [31], and it matched the SEM results. Moreover, the aforementioned results also revealed that the loading of STA would narrow the bandgap of C-ZrO_2 and enhance visible light absorption.

Figure 3c and d displays the N_2 adsorption–desorption isotherms and the BJH pore-size distribution pattern of C-STA@ZrO_2 catalyst. Obviously, the C-STA@ZrO_2 has a type-IV isotherm model, and correspondingly, the BJH pore-size distribution exhibited the presence of mesopores in the composite. According to previous studies [32], STA@UiO-66 has a larger BET surface area (>700 $m^2 \cdot g^{-1}$). When the STA@UiO-66 was calcined, the UiO-66 structure shrinks and collapses, and the produced ZrO_2 formed, resulting in the decreased BET surface area (390.5 $m^2 \cdot g^{-1}$). In addition, pore volume and pore diameter of the C-STA@ZrO_2 catalyst were 0.215 $cm^3 \cdot g^{-1}$ and 2.2 nm, respectively. The aforementioned findings revealed that C-STA@ZrO_2 still possessed mesopore and high BET surface area and pore volume, which is conducive to reducing transfer resistance and enhancing adsorption reactant molecules [33]. Thus, it is supposed that C-STA@ZrO_2 has a better photocatalytic activity in this work.

Also, the XPS spectra of C-STA@ZrO_2 were found, and the results are illustrated in Figure 4. It can be seen from Figure 4a that the C-STA@ZrO_2 catalyst possesses characteristic peaks of O, C, Zr, and W. As shown in Figure 4b, the O 1s peaks of the catalyst are located at 530.1, 531.8, and 533.2 eV, corresponding to W–O, surface hydroxyl oxygen, and weakly absorbed oxygen, respectively [34]. The Zr 3d XPS spectrum in Figure 4c simulated the two peaks around 182.8 and 185.1 eV that are attributed to Zr $3d_{5/2}$ and Zr $3d_{3/2}$, which can prove the existence of Zr^{4+} As shown in Figure 4d, the peaks labeled by 35.6 and 37.7 eV could be assigned to W $4f_{7/2}$ and W $4f_{5/2}$ representing the presence of W^{6+} [35]. Other peaks at 30–32 eV can be observed, which are attributed to the partial decomposition of STA and the formation of an oxide state, and a similar behavior was observed by Xu et al. [36]. The aforementioned results confirmed that the C-STA@ZrO_2 composite has been successfully synthesized.

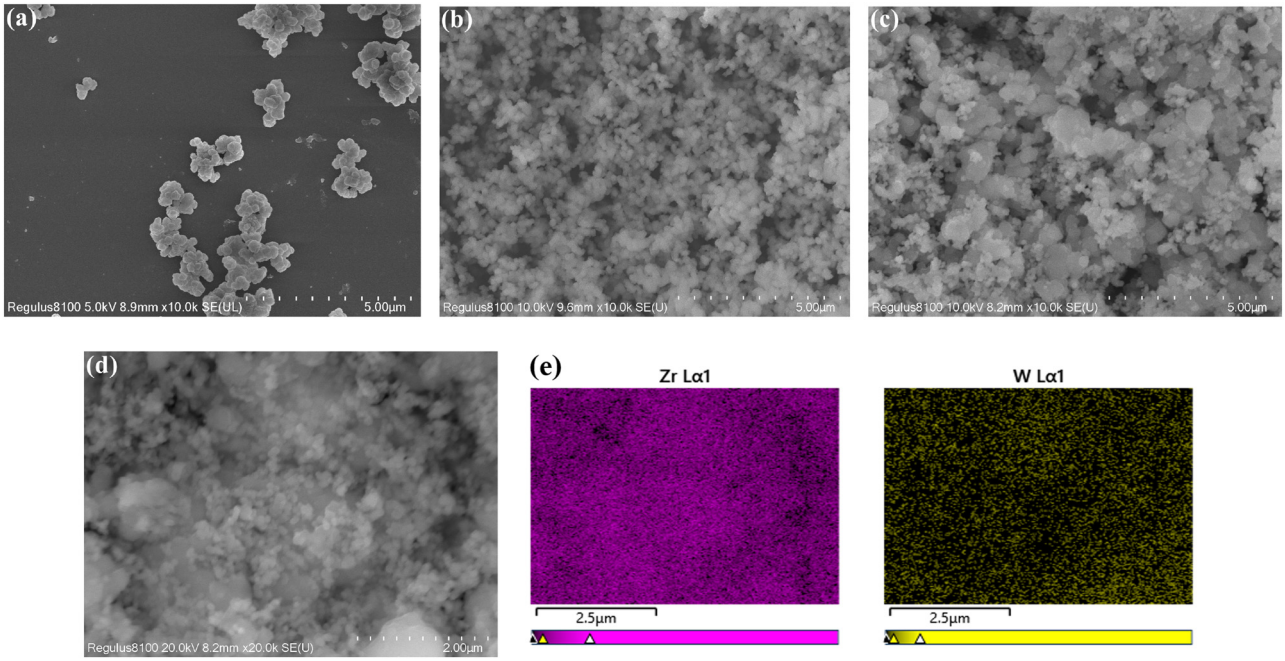

Figure 2: SEM micrographs of UiO-66 (a), C-ZrO_2 (b), C-STA@ZrO_2 (c and d), and (e) the corresponding Zr and W elemental mapping images.

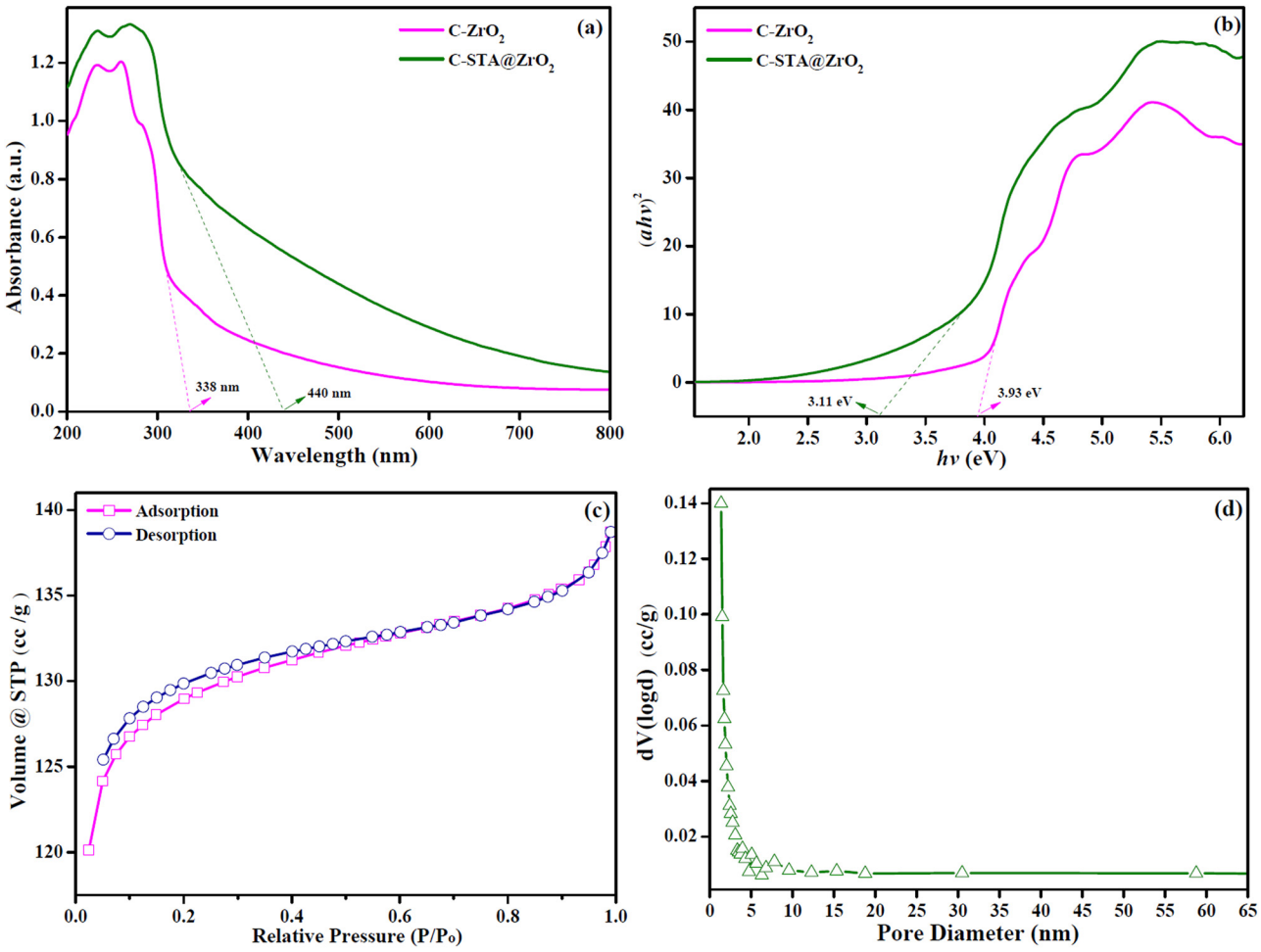

Figure 3: (a) UV-Vis absorption spectra and (b) the Tauc plots of C-ZrO_2 and C-STA@ZrO_2 catalysts; (c) N_2 physisorption isotherm and (d) BJH pore-size distribution of C-STA@ZrO_2 catalyst.

3.2 Photocatalytic activity of synthesized catalysts

The UV absorption spectra during the degradation process are displayed in Figure 5a. It is clear that the absorbance peak intensity of RhB at 554 nm gradually weakened as time increased and the absorption peak is blue-shifted, which can be explained by the step-by-step deethylation process of RhB in the photocatalytic system [37]. Moreover, the photocatalytic performances of C-ZrO_2 and C-STA@ZrO_2 catalysts were studied (Figure 5b). As can be seen in Figure 5b, RhB was hardly decomposed by direct photolysis, and it was also not removed with C-STA@ZrO_2 catalyst under the dark. In addition, it can be seen that C-STA@ZrO_2 has a higher degradation activity than C-ZrO_2 under visible-light irradiation, and the degradation rate of RhB (40 mg·L^{-1}) by C-ZrO_2 and C-STA@ZrO_2 catalysts is approximately 58.2% and 93.9% in 120 min, respectively. As shown in Figure 5c, it is found that the linear relationship between $\ln(C_0/C)$ and reaction time for C-ZrO_2 and C-STA@ZrO_2 catalysts follows the first-order kinetics. Furthermore, the average kinetic rate constants (k) of C-ZrO_2 and C-STA@ZrO_2 are 0.0072 and 0.0231 min^{-1}, respectively, indicating that the k value of C-STA@ZrO_2 is 3.2 times higher than that of C-ZrO_2. The good catalytic performance of C-STA@ZrO_2 catalyst is ascribed to reduce the bandgap of material, the synergistic effects between STA and C-ZrO_2 leading to enhanced photon absorption after the loading of STA.

3.3 Influential factors on the photodegradation of RhB

Figure 6a depicts the effect of catalyst amount on the photodegradation of RhB. From Figure 6a, the improvement in degradation rate was observed with the increase in C-STA@ZrO_2 amount, and the degradation rate was

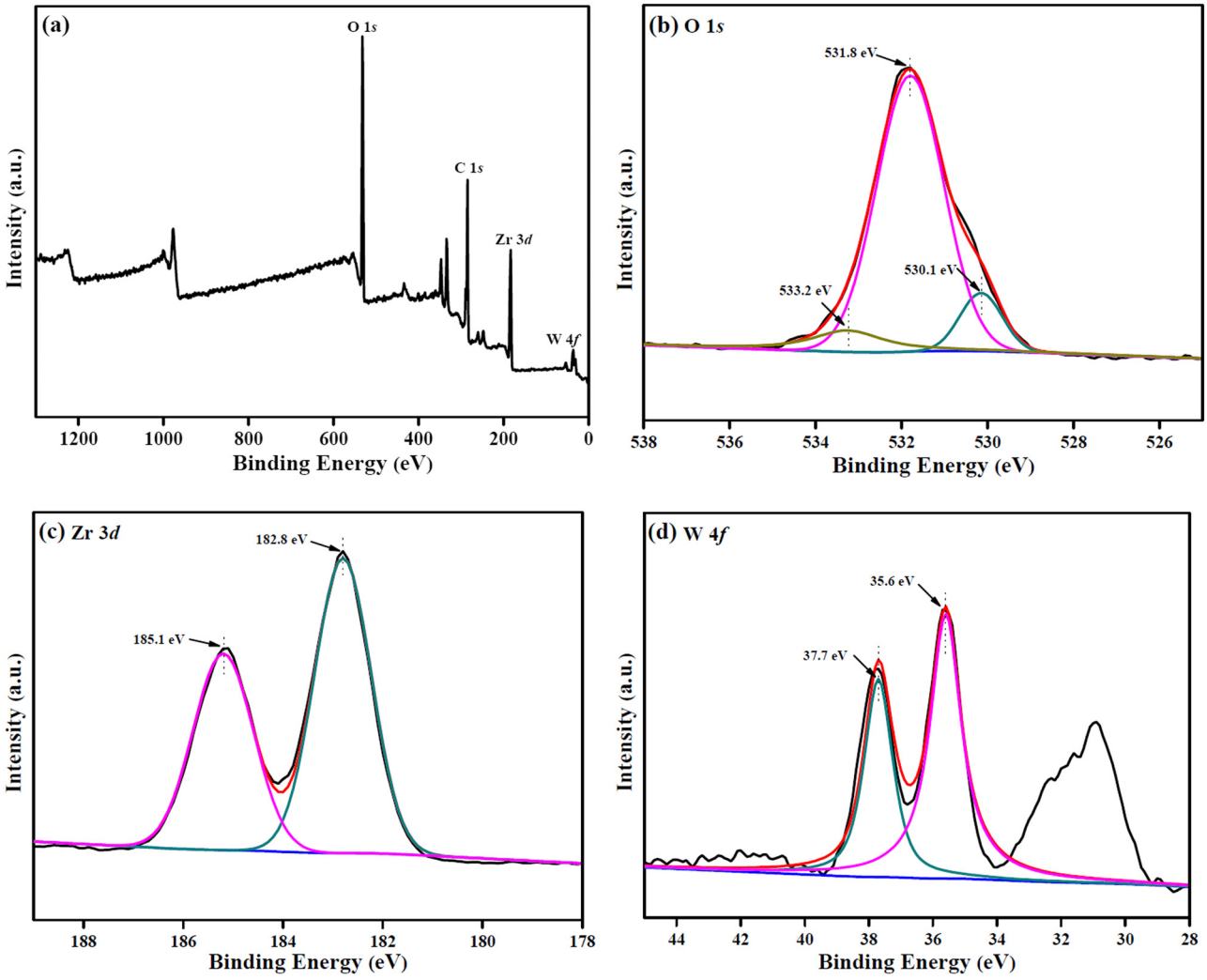

Figure 4: XPS spectrum of the C-STA@ZrO_2: (a) survey spectrum, (b) O 1s, (c) Zr 3d, and (d) W 4f.

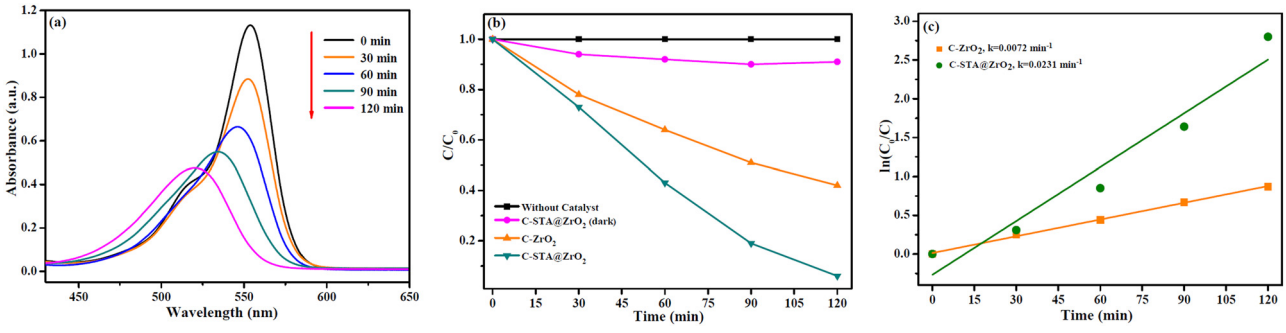

Figure 5: (a) UV-Vis absorption curves of RhB at different times in the presence of C-STA@ZrO_2 catalyst; (b) photocatalytic performance of various catalysts (conditions: catalyst loading = 1.0 g·L^{-1}; initial RhB concentration = 40 mg·L^{-1}). (c) ln(C_o/C) vs time for various catalysts for the degradation of RhB dye.

found to be 93.9% for C-STA@ZrO_2 concentrations of 1.0 g·L^{-1}. This result was attributed to the fact that increasing the catalyst is responsible for the generation of more activated radicals toward RhB degradation [38]. When the amount of the catalyst is further increased, the photocatalytic performance levels off, and this may be attributed to the light reflection and the shielding effect [39]. Therefore, C-STA@ZrO_2 concentrations of 1.0 g·L^{-1} was selected. Additionally, the effect of initial

concentrations of RhB was also examined, as shown in Figure 6b. These experimental results have shown that the photocatalytic rate of C-STA@ZrO_2 decreased from 93.9% to 74.4% as the RhB dye concentration was increased from 40 to 60 mg·L^{-1} in 120 min. This is possible because the active sites on the surface of C-STA@ZrO_2 are available to a particular limit [40]. Therefore, the degradation rate decreases with the increase in the initial concentrations of RhB, and the initial RhB concentrations of 40 mg·L^{-1} are selected for photodegradation.

3.4 Photocatalytic degradation of various dyes

Figure 6c shows the photodegradation of different dyes in the C-STA@ZrO_2 system. Clearly, the degradation rates of CR (40 mg·L^{-1}), AO (40 mg·L^{-1}), MB (20 mg·L^{-1}), and RhB (40 mg·L^{-1}) in the C-STA@ZrO_2 system were 66.6%, 97.4%, 95.8%, and 93.9% after 120 min, respectively. These results suggest that the as-designed C-STA@ZrO_2 system can effectively and photocatalytically degrade organic dyes from wastewater.

3.5 Cycling stability

To evaluate the photocatalytic stability of the C-STA@ZrO_2 catalyst, cycle experiments were performed. After every cycle, the catalyst was separated, washed, and dried for next use. As shown in Figure 6d, it shows that the degradation rate of the C-STA@ZrO_2 catalyst decreased by only 32.8% after three consecutive experiments. Besides, the structures of C-STA@ZrO_2 before and after three cycles

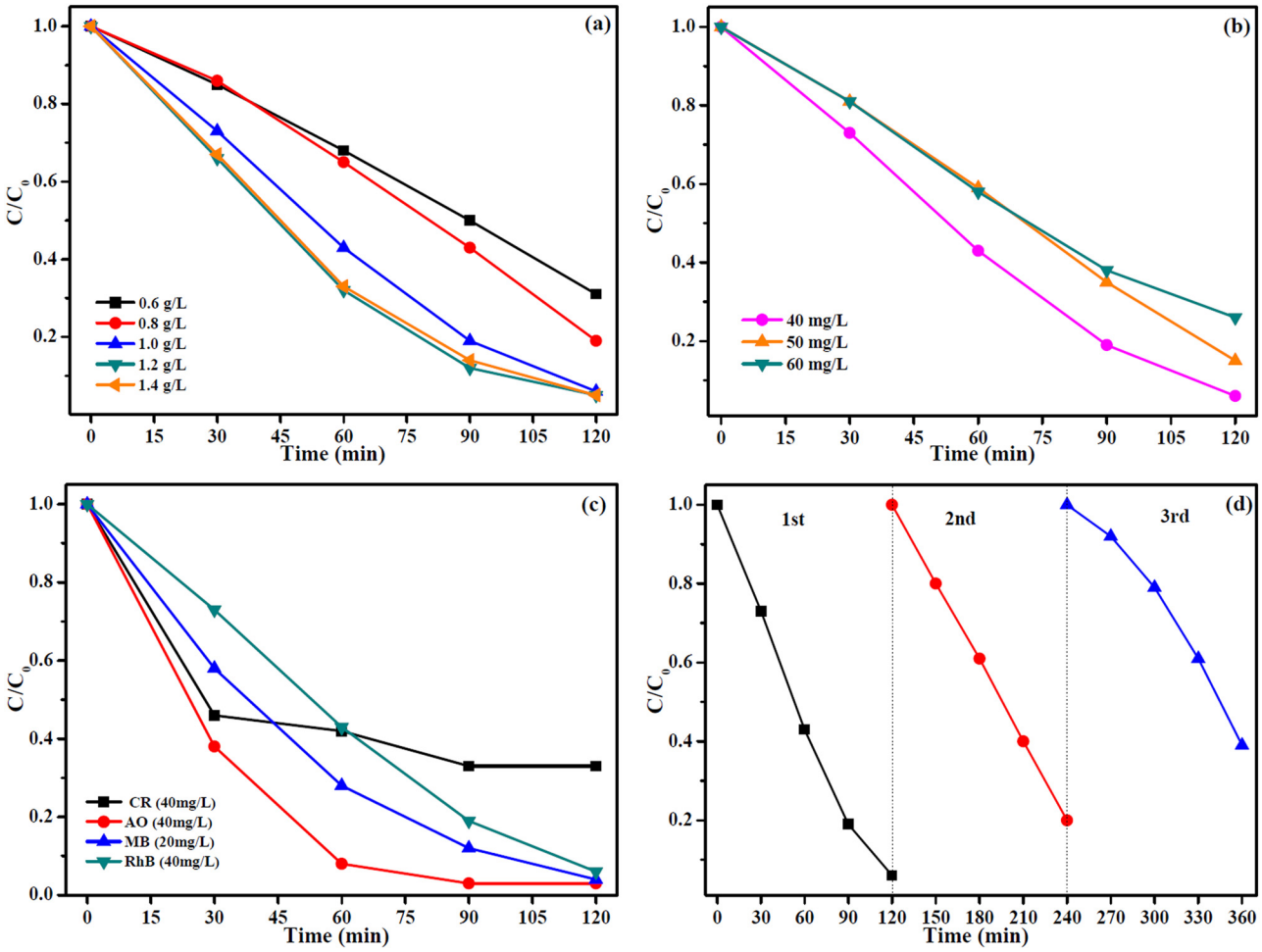

Figure 6: (a) Effect of amount of the C-STA@ZrO_2 catalyst on the photocatalytic degradation of RhB dye (40 mg·L^{-1}). (b) Photocatalytic degradation of RhB dye at various initial dye concentrations in the presence of C-STA@ZrO_2 (1.0 g·L^{-1}) catalyst. (c) Photocatalytic degradation of different dyes in the presence of C-STA@ZrO_2 (1.0 g·L^{-1}) catalyst. (d) Degradation of RhB dye after three cycles in the presence of C-STA@ZrO_2 catalyst (conditions: catalyst loading = 1.0 g·L^{-1}; initial RhB concentration = 40 mg·L^{-1}).

are also presented in Figure A1 and Figure 1. The results reveal that the characteristic XRD and FTIR peaks of the C-STA@ZrO_2 after three cycles were similar to the peaks for the original catalyst, suggesting that the structure of C-STA@ZrO_2 was relatively stable. However, this reduction in catalytic performance might be because of the partial loss of the photocatalyst during the recovery process [41]. Based on the aforementioned discussion, the C-STA@ZrO_2 composite has a relatively good photostability.

3.6 Possible photocatalytic mechanisms

The possible photocatalytic degradation mechanism of RhB by the C-STA@ZrO_2 catalyst under visible light irradiation is shown in Scheme 2. The bandgap values (E_g) of C-ZrO_2 and C-STA@ZrO_2 were estimated by the Tauc plot method in combination with Figure 3b, which were 3.93 and 3.11 eV, respectively, which could be that the loading of STA will induce an intermediate energy level in the bandgap region of C-ZrO_2, and this intermediate energy level allows electrons to move toward it, making the bandgap smaller, which is beneficial for visible light absorption [42]. When the visible light absorbed by C-STA@ZrO_2 is higher than its own forbidden band width, the generation of the photogenerated electrons (e^-) and holes (h^+). e^- jumps from the valence band (VB) of C-STA@ZrO_2 to its conduction band (CB), while h^+ stays on VB. The generated e^- will be captured by O_2 to form $\cdot O_2^-$, and h^+ will react with H_2O to form ·OH. The dyes will react with the generated $\cdot O_2^-$ and ·OH, resulting in dyes that can be easily degraded in water.

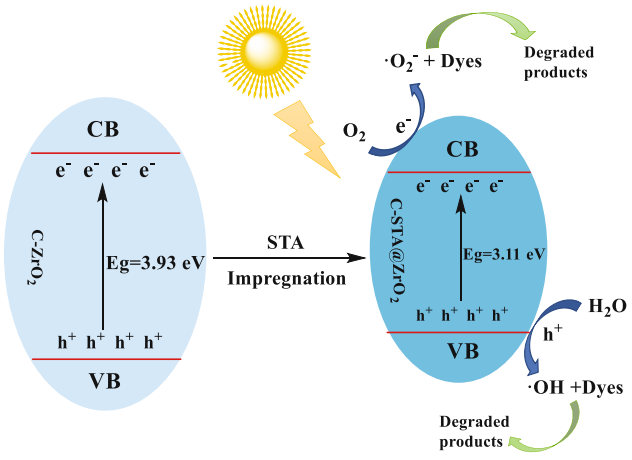

Scheme 2: The possible photocatalytic reaction mechanism of C-STA@ZrO_2 catalyst.

4 Conclusion

In summary, the C-STA@ZrO_2 composite was successfully prepared via the simple method. Through characterization, it was found that the good photocatalytic characteristic of photocatalytic degradation of organic pollutants in water for the C-STA@ZrO_2 catalyst can be attributed to mesopore structure, high BET surface area and pore volume, and the interaction between STA and ZrO_2, which improved the optical response. The degradation efficiency reached 93.9% in 120 min for RhB solution (40 mg·L^{-1}) in the presence of C-STA@ZrO_2 catalyst, and the catalyst can be recycled and reused. The synthesis method proposed in this study can be used to prepare MOF-derived metal oxide skeleton-based hybrids for environmental remediation.

Funding information: This work was financially supported by the Project of Anshun University supporting Doctors Research ([2021]asxybsjj01), the Anshun Science and Technology Planning Project ([2021]1), the 2022 Innovative Entrepreneurship Training Program for Undergraduates of the Guizhou Education Department (202210667017), and the Student Research Training of Anshun University (asxysrt202202).

Author contributions: Jialu Wang: writing – original draft, writing – review and editing, methodology, formal analysis, project administration; Rongfei Yu: methodology, formal analysis; Zhenying Li: methodology, formal analysis; Fen Yang: visualization; Linmin Luo: methodology, formal analysis; Dandan Wang: methodology, formal analysis; Huan Cheng: methodology, formal analysis; Yutao Zhang: visualization; Qiuyun Zhang: writing – review and editing, visualization.

Conflict of interest: The authors declare no conflict of interest.

Data availability statement: The data implemented to support the results of the study are included within the manuscript.

References

[1] Zhang M, Xiong J, Yang H, Wen Z, Chen R, Cheng G. Surface potential/wettability and interface charge transfer engineering of copper-oxide (Cu-MO_x, M = W, Ti, and Ce) hybrids for efficient wastewater treatment through adsorption-photocatalysis synergy. Ind Eng Chem Res. 2020;59:15454–63.

[2] Xiao ZY, Wu R, Shu TT, Wang YX, Li L. Synthesis of Co-doped Fe metal-organic framework MIL-101(Fe,Co) and efficient

degradation of organic dyes in water. Sep Purif Technol. 2023;304:122300.
[3] Zhang QY, Wang DD, Yu RF, Luo LM, Li WH, Cheng JS, et al. Excellent photocatalytic degradation of rhodamine B over Bi_2O_3 supported on Zn-MOF nanocomposites under visible light. Green Process Synth. 2023;12:20228123.
[4] Larowska D, O'Brien JM, Senge MO, Burdzinski G, Marciniak B, Lewandowska-Andralojc A. Graphene oxide functionalized with cationic porphyrins as materials for the photodegradation of rhodamine B. J Phys Chem C. 2020;124:15769–80.
[5] Kurtuldu A, Eşgin H, Yetim NK, Semerci F. Immobilization horseradish peroxidase onto UiO-66-NH_2 for biodegradation of organic dyes. J Inorg Organomet Polym Mater. 2022;32:2901–9.
[6] Soleimani S, Heydari A, Fattahi M, Motamedisade A. Calcium alginate hydrogels reinforced with cellulose nanocrystals for methylene blue adsorption: Synthesis, characterization, and modelling. Ind Crop Products. 2023;192:115999.
[7] Soleimani S, Heydari A, Fattahi M, Motamedisade A. Swelling prediction of calcium alginate/cellulose nanocrystal hydrogels using response surface methodology and artificial neural network. Ind Crop Products. 2023;192:116094.
[8] Mahmoodi NM, Taghizadeh A, Taghizadeh M, Baglou MAS. Surface modified montmorillonite with cationic surfactants: Preparation, characterization, and dye adsorption from aqueous solution. J Environ Chem Eng. 2019;7:103243.
[9] Mousavi SR, Asghari M, Mahmoodi NM. Chitosan-wrapped multiwalled carbon nanotube as filler within PEBA thin film nanocomposite (TFN) membrane to improve dye removal. Carbohydr Polym. 2020;237:116128.
[10] Zhang Y, Hawboldt K, Zhang L, Lu J, Chang L, Dwyer A. Carbonaceous nanomaterial-TiO_2 heterojunctions for visible-light-driven photocatalytic degradation of aqueous organic pollutants. Appl Catal A, Gen. 2022;630:118460.
[11] Nguyen MB, Sy DT, Thoa VTK, Hong NT, Doan HV. Bimetallic Co-Fe-BTC/CN nanocomposite synthesised via a microwave-assisted hydrothermal method for highly efficient Reactive Yellow 145 dye photodegradation. J Taiwan Inst Chem Eng. 2022;140:104543.
[12] Du J, Ma Y, Cui W, Zhang S, Han Z, Li R, et al. Unraveling photocatalytic electron transfer mechanism in polyoxometalate-encapsulated metal-organic frameworks for high-efficient CO_2 reduction reaction. Appl Catal B: Environ. 2022;318:121812.
[13] Jiang X, Zhao D, Chen J, Li W, Li K, Chen C. The synergistic photocatalytic effect of $H_3PW_{12}O_{40}$ and Pt nanoparticles comodified UiO-66-NH_2 on the reduction of aqueous Cr (VI) under original pH. Kinet Catal. 2022;63:470–9.
[14] Wang C, Li AR, Ma YL. Phosphomolybdic acid niched in the metal-organic framework UiO-66 with defects: An efficient and stable catalyst for oxidative desulfurization. Fuel Process Technol. 2021;212:106629.
[15] Zhang QY, Lei YT, Li LY, Lei J, Hu MM, Deng TL, et al. Construction of the novel PMA@Bi-MOF catalyst for effective fatty acid esterification. Sustainable Chem Pharm. 2023;33:101038.
[16] Li YY, Li X, Wang B. Constructing tunable coordinatively unsaturated sites in Fe-based metal-organic framework for effective degradation of pharmaceuticals in water: Performance and mechanism. Chemosphere. 2023;310:136816.
[17] Gouda SP, Dhakshinamoorthy A, Rokhum SL. Metal-organic framework as a heterogeneous catalyst for biodiesel production: A review. Chem Eng J Adv. 2022;12:100415.
[18] Nguyen TQC, Tran HB, Nguyen NK, Nguyen NM, Dang GH. Removal efficiency of dibenzofuran using CuZn-zeolitic imidazole frameworks as a catalyst and adsorbent. Green Process Synth. 2023;12:20228112.
[19] Zhang Y, Wang B, Wang R. Functionally decorated metal-organic frameworks in environmental remediation. Chem Eng J. 2023;455:140741.
[20] Athari M, Fattahi M, Khosravi-Nikou M, Hajhariri A. Adsorption of different anionic and cationic dyes by hybrid nanocomposites of carbon nanotube and graphene materials over UiO-66. Sci Rep. 2022;12:20415.
[21] Jiang H, Xue C, Sun W, Gong Z, Yuan X. Acid regulation of defective sulfonic-acid-functionalized UiO-66 in the esterification of cyclohexene with formic acid. Catal Lett. 2023;153:836–49.
[22] Zhang QY, Hu MM, Wang JL, Lei YT, Wu YP, Liu Q, et al. Synthesis of silicotungstic acid/Ni-Zr-O composite nanoparticle by using bimetallic Ni-Zr MOF for fatty acid esterification. Catalysts. 2023;13:40.
[23] Liu H, Chang Z, Fu J, Hou Z. A CuZn-BTC derived stable Cu/ZnO@SiO_2 catalyst for ethanol dehydrogenation. Appl Catal B: Environ. 2023;324:122194.
[24] Liang H, Zheng Q, Zhang K, Yang Y, He R. Mesoporous CeO_x/MnO_x catalyst derived from Mn-BTC for ozone catalytic decomposition. Appl Catal A, Gen. 2023;653:119080.
[25] Li H, Chu HJ, Ma XL, Wang GR, Liu FS, Guo M, et al. Efficient heterogeneous acid synthesis and stability enhancement of UiO-66 impregnated with ammonium sulfate for biodiesel production. Chem Eng J. 2021;408:127277.
[26] Wang L, Yin GY, Yang YQ, Zhang XD. Enhanced CO oxidation and toluene oxidation on CuCeZr catalysts derived from UiO-66 metal organic frameworks. React Kinet, Mech Catal. 2019;128:193–204.
[27] Zhang QY, Yang TT, Lei DD, Wang JL, Zhang YT. Efficient production of biodiesel from esterification of lauric acid catalyzed by ammonium and silver co-doped phosphotungstic acid embedded in a zirconium metal-organic framework nanocomposite. ACS Omega. 2020;5:12760–7.
[28] Alshorifi FT, Tobbala DE, El-Bahy SM, Nassan MA, Salama RS. The role of phosphotungstic acid in enhancing the catalytic performance of UiO-66 (Zr) and its applications as an efficient solid acid catalyst for coumarins and dihydropyrimidinones synthesis. Catal Commun. 2022;169:106479.
[29] Vo TK, Nguyen MT, Nguyen VC, Kim J. Microwave-assisted synthesis of $MgFe_2O_4$-decorated UiO-66(Zr)-NH_2 composites for collaborative adsorption and photocatalytic degradation of tetracycline. Korean J Chem Eng. 2022;39:2532–41.
[30] Ramasubbu V, Ram Kumar P, Chellapandi T, Madhumitha G, Mothi EM, Sahaya Shajan X. Zn(II) porphyrin sensitized (TiO_2@Cd-MOF) nanocomposite aerogel as novel photocatalyst for the effective degradation of methyl orange (MO) dye. Opt Mater. 2022;132:112558.
[31] Zhou JW, Wang CB, Zhou C, Duo FF, Chu LL, Zhang ML. Self-supporting photocatalyst of 2D Bi_2O_3 anchored on carbon

paper for degradation pollutants. RSC Adv. 2022;12:33449–58.
[32] Zhang QY, Yang TT, Liu XF, Yue CY, Ao LF, Deng TL, et al. Heteropoly acid-encapsulated metal-organic framework as a stable and highly efficient nanocatalyst for esterification reaction. RSC Adv. 2019;9:16357–65.
[33] Mei J, Zhang SH, Pan GJ, Cheng ZW, Chen JR, Zhao JK. Surfactant-assisted synthesis of MOF-derived CeO_2 for low-temperature catalytic *o*-xylene combustion. J Environ Chem Eng. 2022;10:108743.
[34] Wang YS, Shi JJ, Chen XS, Chen MQ, Wang J, Yao JM. Ethyl levulinate production from cellulose conversion in ethanol medium over high-efficiency heteropoly acids. Fuel. 2022;324:124642.
[35] Mulik N, Bokade V. Immobilization of HPW on UiO-66-NH_2 MOF as efficient catalyst for synthesis of furfuryl ether and alkyl levulinate as biofuel. Mol Catal. 2022;531:112689.
[36] Xu F, Liu C, Li JX, Zhan CZ, Xun QN, Zhang WS, et al. Hierarchically porous single catalyst Ru/HPW/UiO-66 with synergistic acid/metal sites for one-pot catalytic synthesis of γ-valerolactone. N J Chem. 2022;46:13047–53.
[37] Lu W, Wang C, Han Y, Bai Y, Wang S, Xi W, et al. An active two-dimensional covalent organic framework for persulfate-assisted high efficiency photocatalytic degradation of rhodamine B. Appl Catal A, Gen. 2022;647:118907.
[38] Xie W, Yuan Y, Jiang W, Zhang SR, Xu GJ, Xu YH, et al. Heterogeneous activation of peroxymonosulfate by stable Co-MOF for the efficient degradation of organic dye pollutants. CrystEngComm. 2022;24:6786–92.
[39] Liu X, Yang Y, Li H, Yang Z, Fang Y. Visible light degradation of tetracycline using oxygen-rich titanium dioxide nanosheets decorated by carbon quantum dots. Chem Eng J. 2021;408:127259.
[40] Maqbool S, Ahmed A, Mukhtar A, Jamshaid M, Rehman AU, Anjum S. Efficient photocatalytic degradation of Rhodamine B dye using solar light-driven La-Mn co-doped Fe_2O_3 nanoparticles. Environ Sci Pollut Res. 2023;30:7121–37.
[41] Shanmuganathan V, Kumar JS, Pachaiappan R, Thangadurai P. Transition metal ion-doped In_2O_3 nanocubes: investigation of their photocatalytic degradation activity under sunlight. Nanoscale Adv. 2021;3:471–85.
[42] Hieu TN, Ha MB, Ya FW, Sheng JY. High flux and hydrogen peroxide-assisted photocatalytic antifouling membranes from coatings of Cu@ZrO_2 onto plasma-grafted PAA/PES. Mater Today Commun. 2022;33:104383.

Appendix

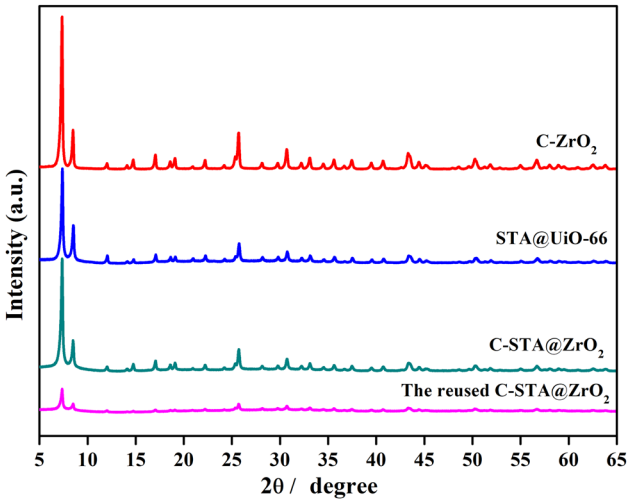

Figure A1: XRD patterns of obtained C-ZrO_2, STA@UiO-66, and C-STA@ZrO_2, and the reused C-STA@ZrO_2 photocatalysts.

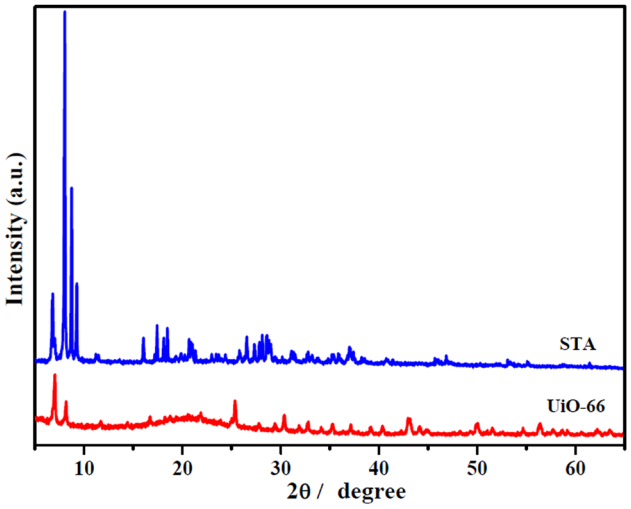

Figure A2: XRD patterns of the STA and UiO-66 samples.